Electronic Supplementary Information

A new class of high capacity cation-disordered oxides for rechargeable lithium batteries: Li-Ni-Ti-Mo oxides

Jinhyuk Lee,[1] Dong-Hwa Seo,[1] Mahalingam Balasubramanian,[2] Nancy Twu,[1] Xin Li,[1,3] and Gerbrand Ceder[4,5*]

[1]Department of Materials Science and Engineering, Massachusetts Institute of Technology, Cambridge, MA 02139, USA

[2]X-ray Science Division, Advanced Photon Source, Argonne National Laboratory, Argonne, Illinois 60439, USA

[3]John A. Paulson School of Engineering and Applied Sciences, Harvard University, Cambridge, MA 02138, USA

[4]Department of Materials Science and Engineering, UC Berkeley, Berkeley, CA 94720, USA

[5]Materials Science Division, Lawrence Berkeley National Laboratory, Berkeley, CA 94720, USA

*Corresponding author. Email: gceder@berkeley.edu

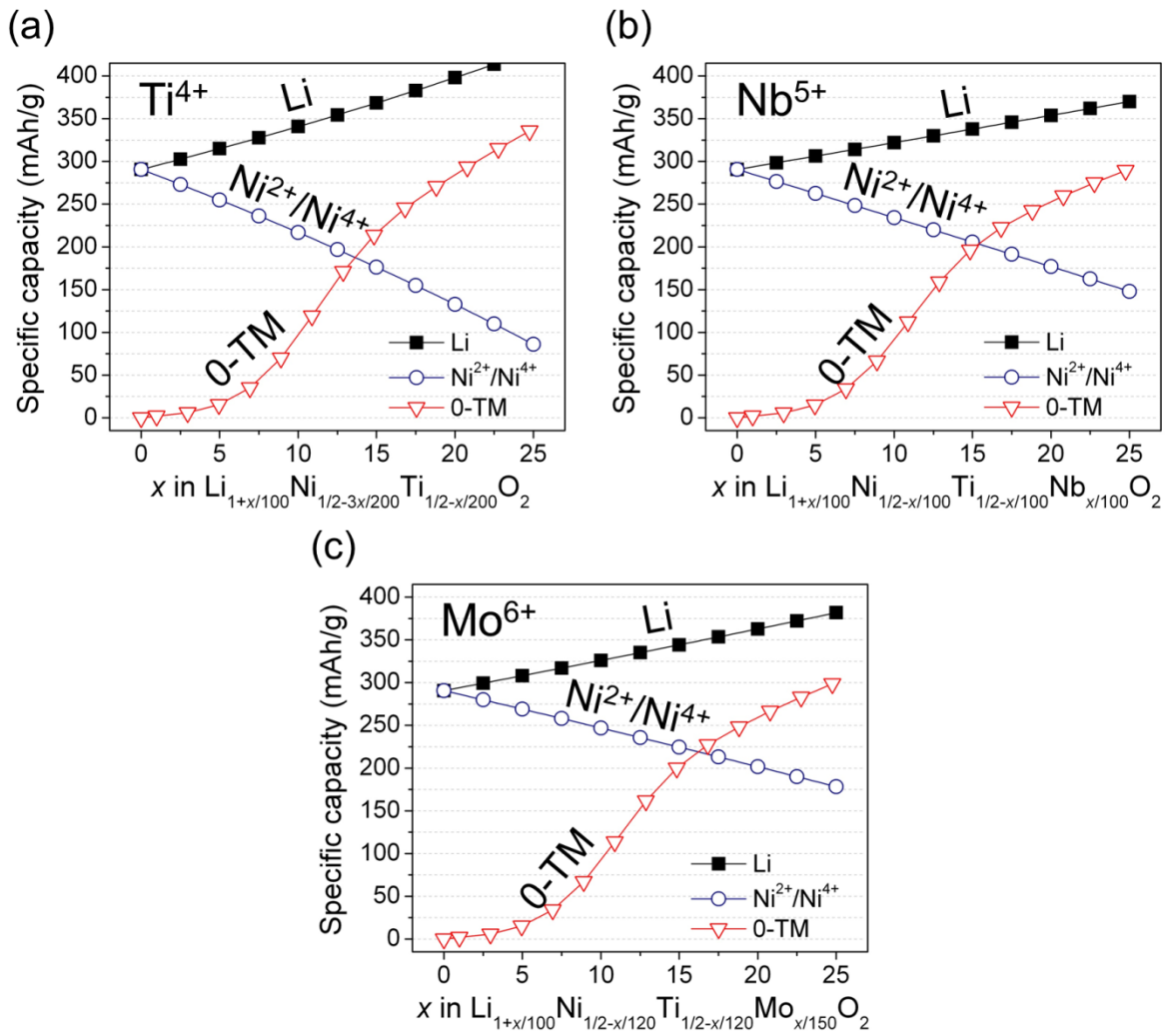

Figure S1. Theoretical capacities are given for solid-solution compounds between $LiNi_{0.5}Ti_{0.5}O_2$ and $Li_{1+\alpha}M_{1-\alpha}O_2$ when M is (a) Ti^{4+} [$\alpha = 1/3$], (b) Nb^{5+} [$\alpha = 0.5$], and (c) Mo^{6+} [$\alpha = 0.6$]. Each figure plots three different capacities: Li capacity that assumes full extraction of available Li^+ ions, Ni^{2+}/Ni^{4+} redox capacity, and 0-TM capacity that is the Li capacity accessible by the percolating 0-TM network. From the figures, it is seen that charge-compensating excess Li^+ with Mo^{6+} sacrifices the least Ni^{2+}/Ni^{4+} capacity. This is because Mo^{6+} has the highest valency among the charge compensators, thus can accommodate excess Li^+ while preserving the most Ni sites for the Ni^{2+}/Ni^{4+} capacity.

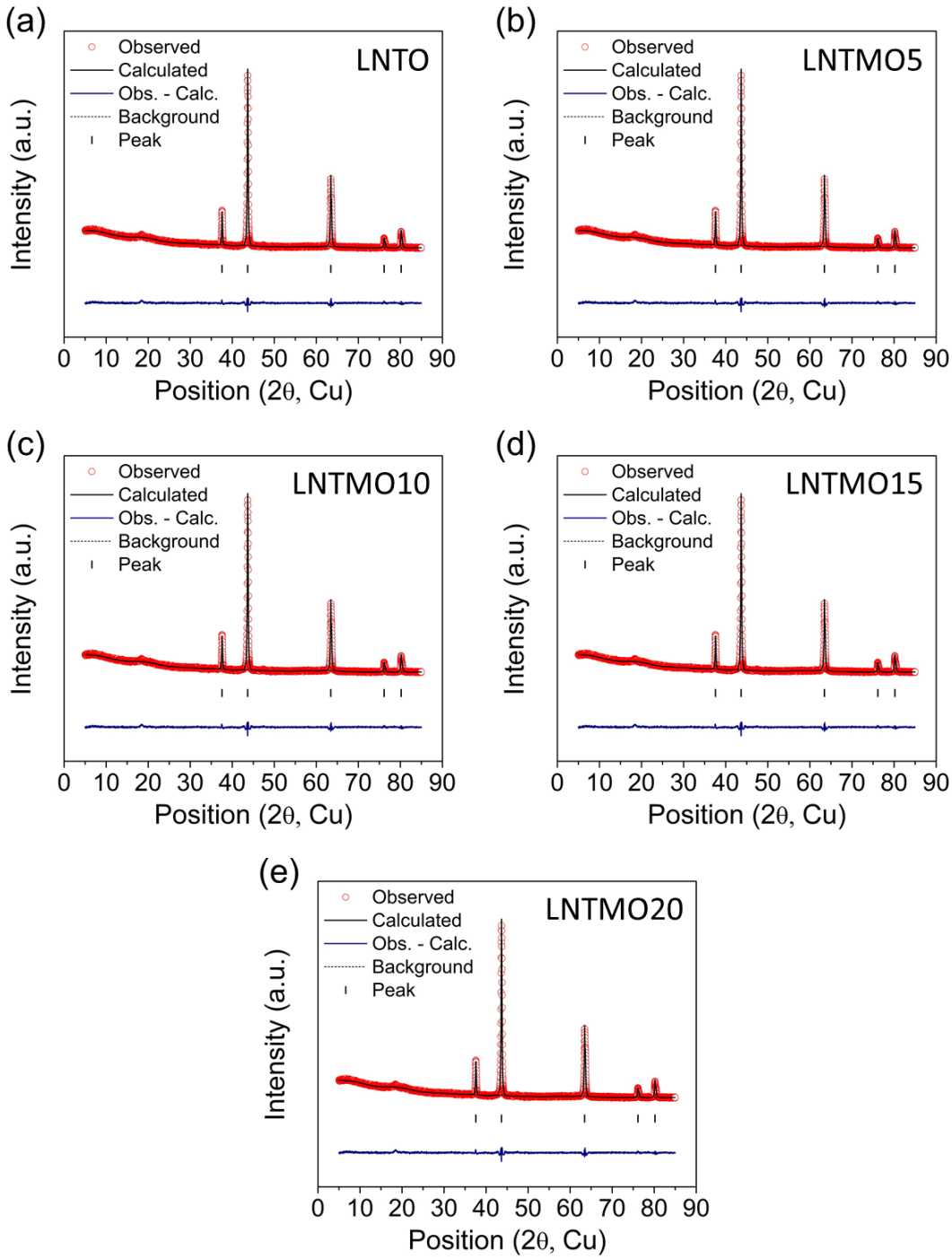

Figure S2. Rietveld refinements on the XRD patterns of (a) $LiNi_{0.5}Ti_{0.5}O_2$ [LNTO], (b) $Li_{1.05}Ni_{11/24}Ti_{11/24}Mo_{1/30}O_2$ [LNTMO5] (c) $Li_{1.1}Ni_{5/12}Ti_{5/12}Mo_{1/15}O_2$ [LNTMO10], (d) $Li_{1.15}Ni_{3/8}Ti_{3/8}Mo_{1/10}O_2$ [LNTMO15], and (e) $Li_{1.2}Ni_{1/3}Ti_{1/3}Mo_{2/15}O_2$ [LNTMO20]: structural parameters from the refinements are listed in Table S1.

Li excess (%)		0	5	10	15	20
Space group		Fm-3m				
Rwp		3.38	6.40	3.79	3.73	2.13
Site 4a (x, y, z) = (0, 0, 0)	Li occupancy	0.497	0.5160	0.5488	0.5750	0.5985
	Ni occupancy	0.262	0.2269	0.2109	0.1899	0.1582
	Ti occupancy	0.254	0.2345	0.2153	0.1925	0.1708
	Mo occupancy	0	0.0163	0.0342	0.0507	0.0671
Site 4b (x, y, z) = (0.5, 0.5, 0.5)	O occupancy	1	1	1	1	1
a (Å)		4.1426	4.1444	4.145	4.1451	4.1452
Volume (Å^3)		71.094	71.186	71.216	71.22	71.226
Derived density (kg/l)		4.39	4.32	4.27	4.22	4.11

Table S1. Structural parameters from the Rietveld refinements in Figure S2: crystallographic information file of Fm-3m $LiFeO_2$ (ICSD collection code 51208) was used as an input file. The atomic occupancies were initially set to the atomic ratio obtained from elemental analysis by direct current plasma emission spectroscopy, based on which the lattice parameters were first refined. Then, we further refined the lattice parameters and the atomic occupancies simultaneously: TM occupancies were first refined, and then Li occupancy was refined. O occupancy did not change after the refinement for all the compounds.

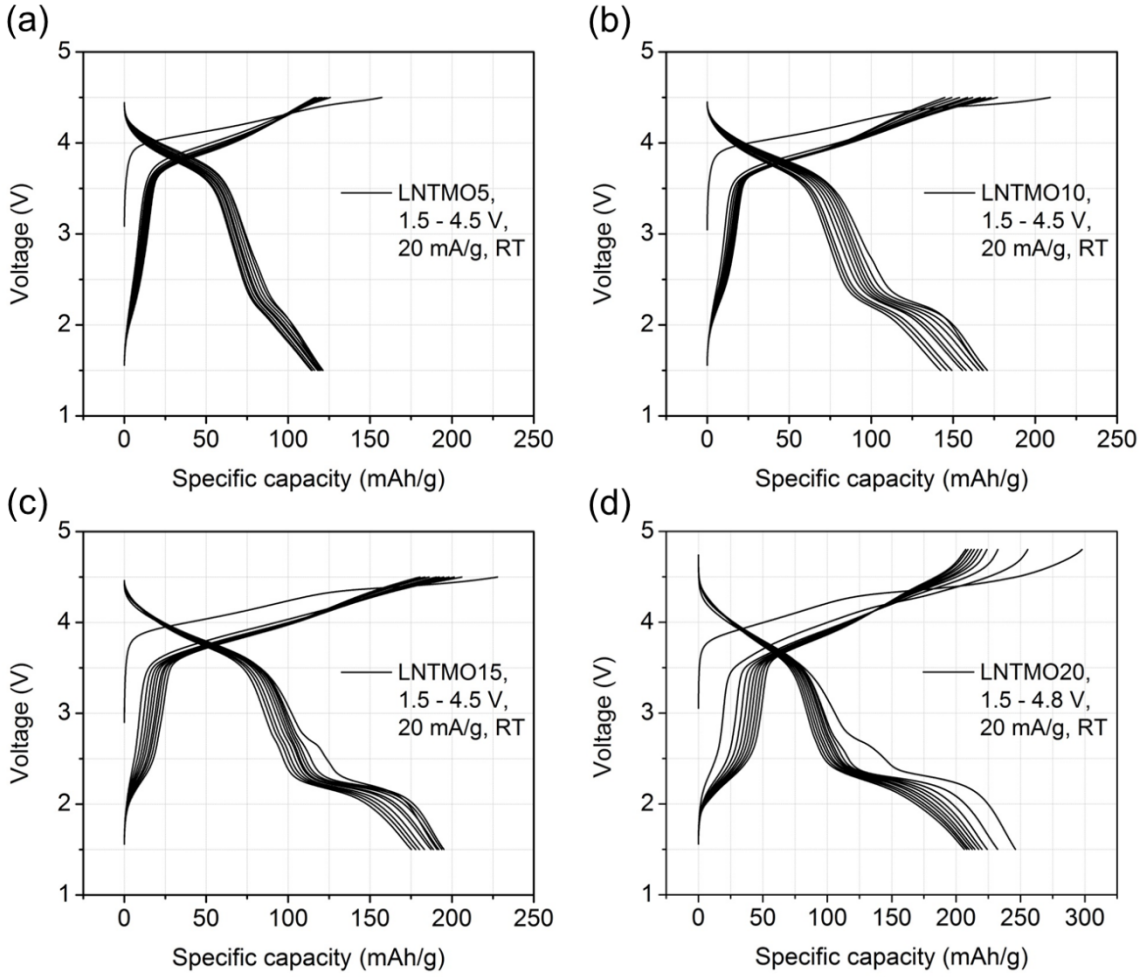

Figure S3. The 10-cycle voltage profiles of (a) $Li_{1.05}Ni_{11/24}Ti_{11/24}Mo_{1/30}O_2$ (LNTMO5), (b) $Li_{1.1}Ni_{5/12}Ti_{5/12}Mo_{1/15}O_2$ (LNTMO10), (c) $Li_{1.15}Ni_{3/8}Ti_{3/8}Mo_{1/10}O_2$ (LNTMO15) when cycled between 1.5−4.5 V at 20 mA/g at room temperature, and (d) the 10-cycle voltage profile of $Li_{1.2}Ni_{1/3}Ti_{1/3}Mo_{2/15}O_2$ when cycled between 1.5−4.8 V at 20 mA/g at room temperature.

Computational supporting data

Computational details

First principles calculations were carried out with density functional theory (DFT) using the spin polarized generalized gradient approximation (GGA).[1] Hubbard U parameters (GGA + U) were used to correct the self-interaction of GGA,[2] using U values of 6.0 eV for Ni and U values of 4.4 eV for Mo.[3] The projector-augmented wave pseudopotentials were used for all energy calculations as implemented to the Vienna *Ab initio* Simulation Package (VASP).[4]
To determine the cation-disordered $Li_{1.2}Ni_{0.33}Ti_{0.33}Mo_{0.13}O_2$ structure, a large number of Li/Ni/Ti/Mo cation orderings were generated by using the genetic algorithm method [5,6] within a 5 × 3 × 2 supercell containing thirty formula units of the monoclinic $LiMO_2$ primitive cell (space group: C2/m). To model the cation-disordered structure, the large supercell was selected and the compositions of cations were fixed to similar composition of $Li_{1.2}Ni_{0.33}Ti_{0.33}Mo_{0.13}O_2$ for every layer along the *c* direction. One hundred Li/Ni/Ti/Mo orderings with lowest electrostatic energy were calculated with GGA+U. Among them, the most stable configuration was selected as the cation-disordered $Li_{1.2}Ni_{0.33}Ti_{0.33}Mo_{0.13}O_2$ structure. The cation-disordered $Li_{0.467}Ni_{0.37}Ti_{0.37}Mo_{0.15}O_2$ structure was also determined by same technique within a 3 × 3 × 3 supercell of the monoclinic $LiMO_2$ primitive cell. The various oxygen/oxygen-vacancy orderings were considered within $Li_{0.467}Ni_{0.33}Ti_{0.33}Mo_{0.13}O_{2-\alpha}$ ($\alpha = 0.2$) to determine the structure of $Li_{0.467}Ni_{0.33}Ti_{0.33}Mo_{0.13}O_{1.8}$ with same technique. The Li/Li-vacancy orderings were also generated for $Li_{1.2-x}Ni_{0.33}Ti_{0.33}Mo_{0.13}O_2$ and $Li_{1.11-x}Ni_{0.37}Ti_{0.37}Mo_{0.15}O_2$ with same methods. Thirty Li/Li-vacancy orderings with lowest electrostatic energy were calculated within GGA+U at each composition. The DFT energies of the most stable configurations at each composition were used to calculate the voltage profile with following equation;

$$\langle V \rangle = -\frac{E\left[Li_{x_1}MO_2\right] - E\left[Li_{x_2}MO_2\right] - (x_1 - x_2)E[Li]}{(x_1 - x_2)F},$$

where E is the DFT energy of the structure and F is the Faraday constant.

The oxidation states were determined by comparing calculated magnetizations (average net moments) of Ni, Ti, Mo and oxygen ions and the number of unpaired spins of Ni^{2+} (2), Ni^{3+} (1), Ni^{4+} (0), Ti^{3+} (1), Ti^{4+} (0), Mo^{5+} (1), Mo^{6+} (0), O^{2-} (0), and O^{-} (1).[7,8] The contributions of

Ni, Ti, Mo and oxygen ions to redox reaction were determined by the change of their magnetization as follows;

$$\text{contribution of A} = \frac{\Delta MA}{\Delta MNi + \Delta MTi + \Delta MMo + \Delta MO},$$

where ΔM is the change of the magnetization between x_1 and x_2.

The oxygen loss potential of $Li_{1.2-x}Ni_{0.33}Ti_{0.33}Mo_{0.13}O_{2-y}$ was also calculated with following equation;

$$\langle V \rangle = -\frac{E\left[Li_{x_1}MO_2\right] - E\left[Li_{x_2}MO_{2-y}\right] - \frac{y}{2}(E_c[O_2] - TS^{exp}_{O_2}(300K)) - (x_1 - x_2)E[Li]}{(x_1 - x_2)F},$$

where E is the DFT energy, $E_c[O_2]$ is the corrected DFT energy of O_2[9],T is temperature (300 K), and $S^{exp}_{O_2}(300K)$ is the entropy of O_2 gas at 300K and 1 atm as obtained from experiments.[10,11] We considered two possible transformed structures for the oxygen loss potential [12] as follows;

(a) $Li_{0.867}Ni_{0.33}Ti_{0.33}Mo_{0.13}O_2 \rightarrow 0.4\ Li + 0.1\ O_2 + Li_{0.519}Ni_{0.37}Ti_{0.37}Mo_{0.15}O_2$

: Oxygen loss with lattice densification

(b) $Li_{0.867}Ni_{0.33}Ti_{0.33}Mo_{0.13}O_2 \rightarrow 0.4\ Li + 0.1\ O_2 + Li_{0.467}Ni_{0.33}Ti_{0.33}Mo_{0.13}O_{1.8}$

: Oxygen loss with oxygen vacancy formation

Based on the above equations, we can find that the thermodynamically more favorable reaction will be the one with lower-energy reaction products (densified $Li_{0.519}Ni_{0.37}Ti_{0.37}Mo_{0.15}O_2$ vs. $Li_{0.467}Ni_{0.33}Ti_{0.33}Mo_{0.13}O_{1.8}$ with oxygen vacancies). Based on our calculations, we find that the densified $Li_{0.519}Ni_{0.37}Ti_{0.37}Mo_{0.15}O_2$ structures are energetically more stable than the $Li_{0.467}Ni_{0.33}Ti_{0.33}Mo_{0.13}O_{1.8}$ structures with oxygen vacancies even though they have a same supercell-composition of $Li_{14}Ti_{10}Ni_{10}Mo_4O_{54}$. The energy difference between these two structures is 105 meV per Li_xMO_2 formula unit (Fig. S4). Thus, the oxygen loss potential in Figure S5 is derived from reaction (a): oxygen loss with lattice densification.

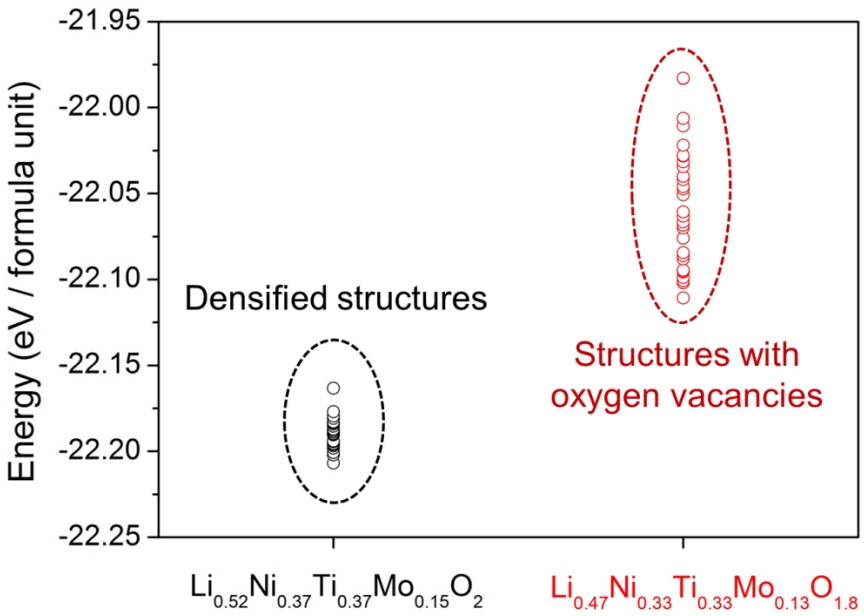

Figure S4.The calculated energies of densified $Li_{0.52}Ni_{0.37}Ti_{0.37}Mo_{0.15}O_2$ structures and $Li_{0.47}Ni_{0.33}Ti_{0.33}Mo_{0.13}O_{1.8}$ structures with oxygen vacancies. It is seen that the energies of the densified $Li_{0.52}Ni_{0.37}Ti_{0.37}Mo_{0.15}O_2$ structures are lower than those of $Li_{0.47}Ni_{0.33}Ti_{0.33}Mo_{0.13}O_{1.8}$ structures with oxygen vacancies. This indicates that oxygen loss with densification is thermodynamically more favorable than that with oxygen vacancies in the lattice.

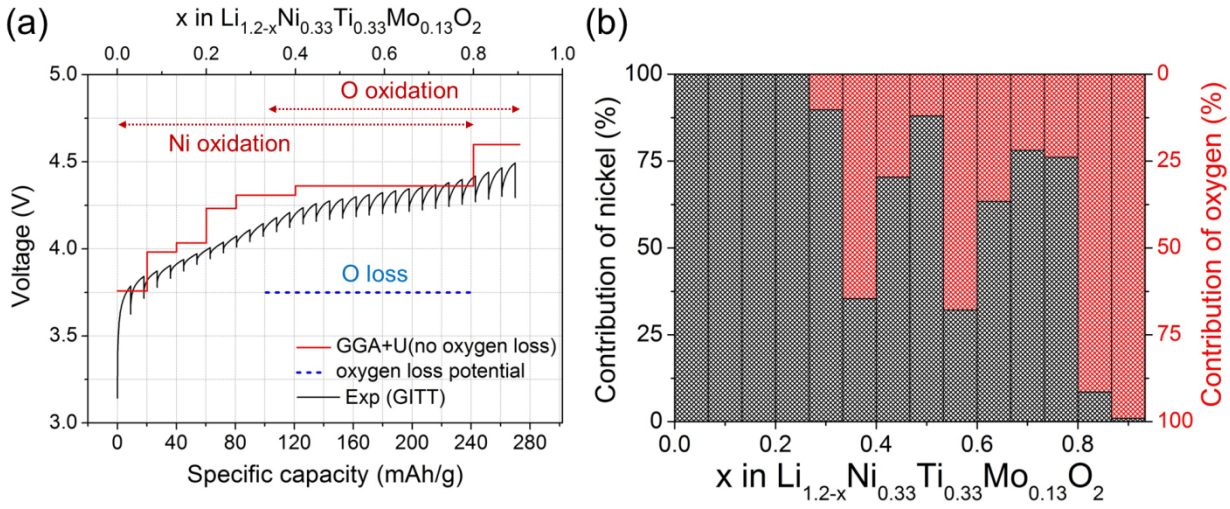

Figure S5. (a) The voltage profiles of $Li_{1.2-x}Ni_{0.33}Ti_{0.33}Mo_{0.13}O_2$. The black curve is an experimental profile from the galvanostatic intermittent titration test (GITT) during the first charge, and the red line is calculated voltage profile of $Li_{1.2-x}Ni_{0.33}Ti_{0.33}Mo_{0.13}O_2$ that assumes no oxygen loss during the first charge: the dotted red arrows specify the region of Ni oxidation and O oxidation. Finally, the dashed blue line indicates the oxygen-loss potential of $Li_{1.2-x}Ni_{0.33}Ti_{0.33}Mo_{0.13}O_{2-y}$. (b) The calculated contribution of Ni [black] and oxygen [red] oxidation upon delithiating $Li_{1.2-x}Ni_{0.33}Ti_{0.33}Mo_{0.13}O_2$ when no oxygen loss is assumed (the red curve in Figure S5a).

To further understand the behavior of $Li_{1.2-x}Ni_{0.33}Ti_{0.33}Mo_{0.13}O_2$ (LNTMO20) during cycling, we investigated the redox mechanism of LNTMO20 with DFT calculations. Figure S5a compares the computed first charge voltage profiles of LNTMO20 against the experimental profile. The red curve is the computed profile assuming no oxygen loss from the crystal structure of LNTMO20 upon first charge. The blue line is the computed voltage, which assumes that partially-delithiated LNTMO20 ($Li_{0.867}Ni_{0.33}Ti_{0.33}Mo_{0.13}O_2$) loses oxygen (-0.1 O_2) upon further charge (-0.4 Li), leading to a densified disordered phase of $Li_{0.52}Ni_{0.37}Ti_{0.37}Mo_{0.15}O_2$ that is thermodynamically more stable than a disordered phase with oxygen vacancies ($Li_{0.47}Ni_{0.33}Ti_{0.33}Mo_{0.13}O_{1.8}$) (Fig. S4). Finally, the black curve is the experimental profile from GITT. Figure S5b shows the contribution of Ni and oxygen oxidation upon delithiating LNTMO20 when no oxygen loss is assumed, which results in the red profile in the Figure S5a.

In general, the experimental voltage (black) is lower than the calculated voltage without oxygen loss (red) and higher than the calculated voltage with oxygen loss (blue). The much lower (calculated) voltage from oxygen loss than without oxygen loss shows that there is a clear driving force for oxygen loss from LNTMO20 after a certain level of delithiation. The calculated voltage with oxygen loss is quite lower than the experimental profile, implying that the actual first charge mechanism is likely to include some degree of oxygen loss based on the thermodynamic driving force. Note that the oxygen loss mechanism in experiments can be more complicated than what is assumed in our calculations. Therefore, there can be a discrepancy in the oxygen loss voltage between the calculations and experiments.

Although there is a clear driving force for oxygen loss after a certain level of delithiation, the computed voltage without oxygen loss (thus with Ni and O oxidation only) is also within an experimental voltage window of 1.5−4.5 V (or 1.5−4.8 V). Thus, not to mention the Ni oxidation which is experimentally confirmed by Ni XANES (Fig. 9a), oxygen oxidation can also take place at high voltage along with oxygen loss. It is notable that the oxygen oxidation is predicted to occur before Ni^{2+} becomes completely oxidized to Ni^{4+} (Fig. S5b). In theory, the full Ni^{2+}/Ni^{4+} capacity allows for 0.66 Li delithiation. However, oxygen oxidation already takes place after ~0.35 Li delithiation, indicating an overlap between Ni 3*d* and O 2*p* bands in LNTMO20.

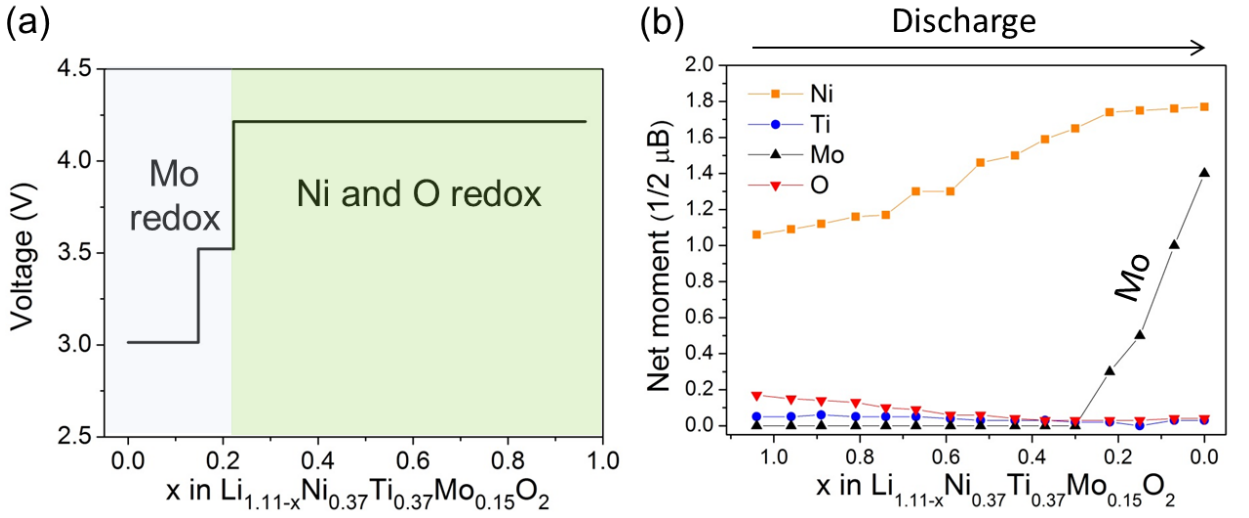

Figure S6. (a) The calculated voltage profile of $Li_{1.11-x}Ni_{0.37}Ti_{0.37}Mo_{0.15}O_2$. (b) The average net moments of Ni, Ti, Mo and oxygen ions in $Li_{1.11-x}Ni_{0.37}Ti_{0.37}Mo_{0.15}O_2$ (x = 0, 0.074, 0.148, 0.222, 0.296, 0.370, 0.444, 0.519, 0.593, 0.667, 0.741, 0.815, 0.889, 0.963 and 1.037) from calculations.

After oxygen loss, not only Ni^{3+}, Ni^{4+}, and O^{-}, but also Mo^{6+} and Ti^{4+} can be reduced upon discharge. To study which species (Mo^{6+} vs. Ti^{4+}) is first reduced after oxygen loss, we computationally studied the redox mechanism of $Li_{1.11-x}Ni_{0.37}Ti_{0.37}Mo_{0.15}O_2$, which models a possible densified disordered phase of LNTMO20 after some degree of oxygen loss. Figure S6a shows the calculated voltage profile of $Li_{1.11-x}Ni_{0.37}Ti_{0.37}Mo_{0.15}O_2$ (assuming no further oxygen loss upon charging) and Figure S6b shows the (calculated) average net moments of Ni, Ti, Mo and oxygen ions in $Li_{1.11-x}Ni_{0.37}Ti_{0.37}Mo_{0.15}O_2$ at each composition. The average net moment of Ni ions continuously increases from 1.06 to 1.77 as x decreases from 1.04 to 0.22, indicating reduction of $Ni^{\sim 3+}$ to Ni^{2+} on average. Simultaneously, the average net moment of O ions decreases from 0.17 to 0.03 as x decreases from 1.04 to 0.44, indicating reduction of $O^{\sim 1.8-}$ to O^{2-} on average. Although the net moments of Ti ions remain unchanged for the whole compositions in $Li_{1.11-x}Ni_{0.37}Ti_{0.37}Mo_{0.15}O_2$, the average net moment of Mo ions rapidly increases as x decreases from 0.22 to 0. This indicates that Mo reduction occurs before Ti reduction but after O and Ni reduction. Thus, for the Ti reduction to occur after oxygen loss, it is likely that Mo reduction has already taken place to some degree.

References

1. J. P. Perdiew,K. Burke and M. Ernzerhof, Generalized Gradient Approximation Made Simple, *Phys. Rev. Lett.*1996, **77**, 3865.
2. S. L. Dudarev, G. A. Botton, S. Y. Savrasov, C. J. Humphreys and A. P. Sutton, Electron-Energy-Loss Spectra and the Structural Stability of Nickel Oxide: An LSDA+U Study, *Phys. Rev. B*, 1998, **57**, 1505.
3. A. Jain, G. Hautier, S. P. Ong, C. J. Moore, C. C. Fischer, K. A. Persson, and G. Ceder, *Phys. Rev. B*, 2011, **84**, 045115.
4. G. Kresse and J. Furthmuller, Efficiency of *Ab-Initio* Total energy Calculations for Metals and Semiconductors Using a Plane-Wave Basis Set, *Comput. Mater. Sci.*, 1996, **6**, 15–50.
5. S. M. Woodley, P. D. Battle, J. D. Gale and C. R. A. Catlow, The Prediction of Inorganic Crystal Structures Using a Genetic algorithm and Energy Minimisation, *Phys. Chem. Chem. Phys.*1999, **1**, 2535–2542.
6. S. M. Woodley and R. Catlow, Crystal Structure Prediction from First Principles, *Nature Mater.* 2008, **7**, 937–946.
7. J. Reed,G. Ceder and A.Van Der Ven, Layered-to-Spinel Phase Transition in Li_xMnO_2, *Electrochem. Solid State Lett.*,2001, **4**, A78–A81.
8. B. J. Hwang, Y. W. Tsai, D. Carlier and G. Ceder, A Combined Computational/Experimental Study on $LiNi_{1/3}Co_{1/3}Mn_{1/3}O_2$, *Chem. Mater.*2003, **15**, 3676–3682.
9. L. Wang, T. Maxisch and G. Ceder, Oxidation Energies of Transition Metal Oxides within the GGA+U Framework, *Phys. Rev. B*, 2006, **73**, 195107.
10. M. W. Chase, *NIST-JANAF Thermodynamical Tables*; American Chemical Society: New York, 1998; Vol. 12.
11. S. Kang, Y. Mo, S. P. Ong and G. Ceder, Nanoscale Stabilization of Sodium Oxides: Implications for Na-O_2 Batteries, *Nano Lett.*,2014**, 14,** 1016**–**1020.
12. N. Tran, L. Croguennec, M. Ménétrier, F. Weill, P. Biensan, C. Jordy and C. Delmas, Mechanisms Associated with the "Plateau" Observed at High Voltage for the Overlithiated $Li_{1.12}(Ni_{0.425}Mn_{0.425}Co_{0.15})_{0.88}O_2$ System, *Chem. Mater.*, 2008, **20**, 4815–4825.